Chaotic escape from an open vase-shaped cavity. I. Numerical and experimental results

Jaison Novick,[1,*] Matthew L. Keeler,[2] Joshua Giefer,[2] and John B. Delos[1]
[1]*Department of Physics, College of William and Mary, Williamsburg, Virginia 23187-8795, USA*
[2]*Department of Physics, University of Minnesota, Morris, Morris, MN 56267, USA*
(Received 6 November 2010; published 18 January 2012)

We present part I in a two-part study of an open chaotic cavity shaped as a vase. The vase possesses an unstable periodic orbit in its neck. Trajectories passing through this orbit escape without return. For our analysis, we consider a family of trajectories launched from a point on the vase boundary. We imagine a vertical array of detectors past the unstable periodic orbit and, for each escaping trajectory, record the propagation time and the vertical detector position. We find that the escape time exhibits a complicated recursive structure. This recursive structure is explored in part I of our study. We present an approximation to the Helmholtz equation for waves escaping the vase. By choosing a set of detector points, we interpolate trajectories connecting the source to the different detector points. We use these interpolated classical trajectories to construct the solution to the wave equation at a detector point. Finally, we construct a plot of the detector position versus the escape time and compare this graph to the results of an experiment using classical ultrasound waves. We find that generally the classical trajectories organize the escaping ultrasound waves.

DOI: 10.1103/PhysRevE.85.016205 PACS number(s): 05.45.Pq, 05.45.Mt, 42.15.Dp, 42.65.Wi

I. INTRODUCTION

Chaotic transport occurs in chemical reactions, as a temporarily formed complex breaks up into products (or returns to reactants) [1–6], in scattering from three circular discs [7,8], in the emission of light from microbeads [9–19] or the emission of microwaves from cavities, [19–25] in the ionization of excited hydrogen atoms by microwave radiation [26], in the escape of atoms from traps [27], in the ionization of atoms in static electric and magnetic fields [28–33], in the mixing of fluids or granular materials [34–41], in the diffusion of electrons through arrays of quantum dots [42–46] or through other periodic potentials [47–51], in ocean currents [52–58], and in transport of satellites (or asteroids or meteors) through the solar system [59–61].

The defining characteristic of chaotic transport is sensitive dependence on initial conditions. This sensitive dependence manifests itself in graphs of the time to escape vs initial conditions: such graphs display fractal structure within structure at all levels of resolutions (many of the colorful representations of fractals are made from calculations of escape times in chaotic two-dimensional maps) [62–64]. In earlier work [25,27,31,33,65,67] a geometrical and topological framework was developed for describing the structure of escape-time graphs in systems with two degrees of freedom (2-dof = four dimensional phase space). This approach, called homotopic lobe dynamics, examines the number of bounces from the walls of the vase that a path will have before escaping (or more generally, the number of intersections with a surface of section before escape); it shows that a graph of bounces before escape vs initial direction of motion must show fractal structure, and it predicts a minimal topologically required subset of this fractal. Since the first presentation of this theory [65,66], two improvements to the theory have been developed [25,67], each predicting a larger subset of the fractal.

Here, we study escape of light or sound or microwaves from a two-dimensional vase-shaped cavity. A point source on the boundary sends out rays; these rays undergo specular reflection from the sides of the vase, and eventually most of them escape. This does not sound like a problem that would require 21st century mathematics for its solution. In fact, however, 21st century mathematics are not yet adequate for a complete description of this system. The vase is one of the simplest systems in which the dynamics shows all the complexity of 2-dof chaotic transport and on which clean and precise measurements can be made.

We began the study of this system in Ref. [68], and many of the concepts and methods we use here are similar to those described therein. New in this paper are the following aspects: (1) we now study a vase with a wider neck; this allows us to go deeper into the fractal structure for a given number of reflections from the boundary of the vase. (2) In Ref. [68], we reported the total flux of particles out of the mouth of the vase. Here, we report the flux density into individual detectors across the mouth of the vase. (3) We have constructed an experimental realization of this vase using ultrasound, and we have verified the early part of the structure that is predicted theoretically. (4) In Ref. [68] and in the ultrasound observations, we examine a point source of short pulses and compute or measure the time required for the pulse to arrive at a detector. In microwave experiments [20–22], it may be easier to use a source of steady waves having controlled frequency. Here, we compute the waves arriving at a detector from such a source. The Fourier transform from frequency to time gives results which are consistent with pulsed measurements. (5) In the accompanying paper [69], we apply one of the recent improvements of homotopic lobe dynamics, using it to predict a minimal part of the fractal structure that appears in the escape-time plot for this vase.

II. THE VASE, THE SURFACE OF SECTION, AND THE HOMOCLINIC TANGLE

In this section (and in the supplementary material [70]), we define the shape of the vase, and we display some escape-time

*Corresponding author: jaisonnovick@gmail.com

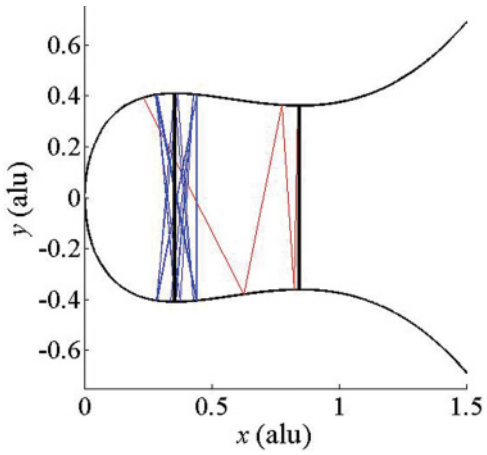

FIG. 1. (Color online) The vase for $A = 0.75$ and $w = 0.75$. The stable and unstable periodic orbits (SPO and UPO) are plotted in thick lines (black online). A stable orbit surrounding the SPO is shown (blue online; dark grey print). Another trajectory (red online; medium grey print) starts near the UPO and rapidly falls away from the UPO. This path is representative of a continuous family of trajectories that makes up the stable manifold of the unstable fixed point in the surface of section (see Fig. 4). Figure 1 and most of our simulations use arbitrary length units, which we will abbreviate as alu. We choose corresponding arbitrary time units (abbreviated as atu) such that the speed along the paths in Fig. 1 is 1 alu (atu^{-1}).

graphs. Then we show how to obtain a discrete map between successive reflections from the continuous paths in the vase. Finally, we define and display a homoclinic tangle, which governs the structure of the escape-time graphs.

A. The shape of the vase

We consider a chaotic, open vase-shaped cavity. The vase walls are given by Eq. (1):

$$y(x) = \pm\sqrt{x}\left(\frac{w}{2} + A(x-1)^2\right) = \pm f(x). \tag{1}$$

The parameter w controls the neck's width, and A controls how much the vase lips flare outward. We chose $A = 0.75$ and $w = 0.75$ as these result in an early onset of chaos. The vase constructed from these parameters and several regular trajectories found in the vase are shown in Fig. 1. In Fig. 1, we have labeled the axes in units of alu, which stands for arbitrary length units. Equation (1) is not defined with respect to any system of units, such as SI units. For comparison to an experiment, the inputs and outputs in Eq. (1) have to be rescaled.

Trajectories are straight lines between specular reflections from the boundary walls. In Fig. 1, the thick vertical line segments (black online) in the vase's bowl and neck represent stable and unstable periodic orbits (SPO and UPO, respectively). The SPO is surrounded by a region of trapped orbits, one of which is shown in Fig. 1 (blue online). The trajectory (red online) starting near and falling away from the UPO shows how trajectories are repelled away from the UPO. The UPO is most important to our analysis, as all trajectories intersecting the UPO escape without return due to the outward flaring of the vase's lips and the lack of reflectors other than the two boundary walls.

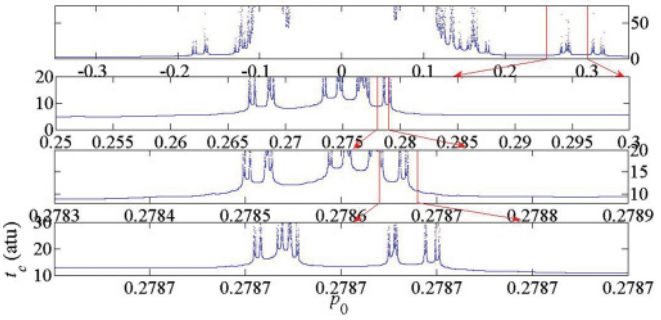

FIG. 2. (Color online) The top figure shows the continuous escape time (t_c) versus the initial momentum (p_0) for a burst launched from the boundary point $\boldsymbol{r}_0 = (0.3, 0.4067)$ to a vertical line detector placed at $x = 1.5$. The second row features a magnification of the region bounded by vertical (red online) lines near the right-hand side of the top figure. The third and fourth rows are magnifications of the regions bounded by the vertical (red online) lines in the second and third rows, respectively.

Numerical computation of trajectories is described in the supplementary material [70]. For our simulations, we launch a burst of trajectories from a point source on the upper boundary at $\boldsymbol{r}_0 = (0.3, 0.4067)$. To the right of the UPO, at $x = 1.5$ alu, we imagine a vertical line detector spanning the space between the boundary walls. All trajectories that pass through the UPO are absorbed at the vertical line detector. We record the propagation time between launch and absorption and plot this escape time versus the initial velocity component parallel to the tangent to the vase at the source point (called the initial momentum p_0 in Fig. 2). The escape times of the chaotic trajectories are organized into infinite sequences of U-shaped regions called icicles. Each icicle represents the escape times for a family of chaotic trajectories. Sequences of icicles can be found at all levels of resolution [65,66,68].

B. Surface of section

The structure underlying the escape time plots in Fig. 2 is revealed in a discrete representation. At each reflection from the boundary, a surface of section is defined in the standard way, using the arclength along the boundary and the momentum parallel to the boundary's tangent line at the reflection point. More specifically, at any reflection point $\boldsymbol{r} = (x, y)$, the coordinate is defined as the signed arclength along the boundary between the origin and the reflection point:

$$q(x) = \int_0^{y(x)} dy \sqrt{1 + \left(\frac{dx}{dy}\right)^2}, \quad x < x_{\text{cutoff}}, \tag{2}$$

$$q(x) = \int_0^{y(x_{\text{cutoff}})} dy \sqrt{1 + \left(\frac{dx}{dy}\right)^2} + \int_{x_{\text{cutoff}}}^{x} dx \sqrt{1 + \left(\frac{dy}{dx}\right)^2}, \quad x > x_{\text{cutoff}}. \tag{3}$$

To define the momentum p, we construct the unit tangent vector $\boldsymbol{T}(\boldsymbol{r}_0)$ and calculate the component of the incoming and outgoing velocity parallel to this vector:

$$p = \boldsymbol{v}_{\text{incoming}} \cdot \boldsymbol{T}(\boldsymbol{r}_0) = \boldsymbol{v}_{\text{outgoing}} \cdot \boldsymbol{T}(\boldsymbol{r}_0). \tag{4}$$

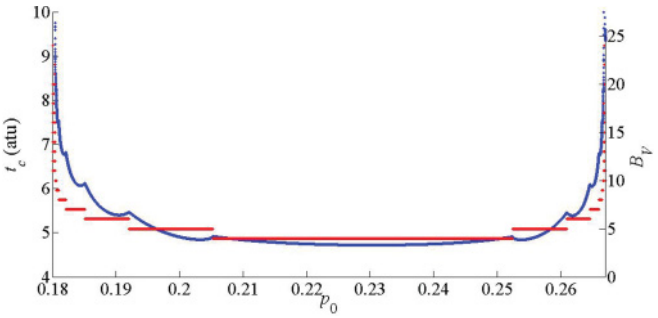

FIG. 3. (Color online) Continuous escape time (left vertical axis and plotted in blue online, dark grey print) and bounces to escape the vase (B_V, right vertical axis and plotted in red online, medium grey print) versus the initial momentum for a single icicle. Discontinuities in slope of the escape time curve occur at the points at which the number of bounces changes by one. This icicle corresponds to escape segment E_1 in Fig. 5.

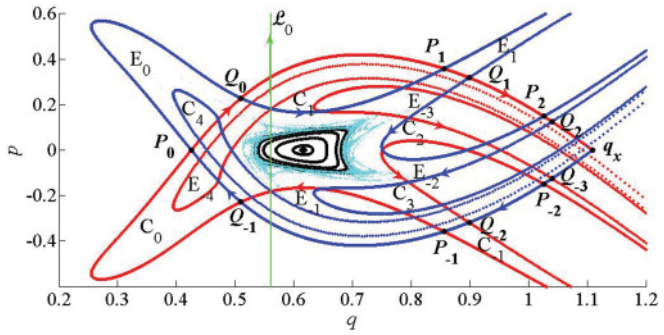

FIG. 4. (Color online) Homoclinic tangle that controls chaotic transport in the vase. The oriented curves attached to the point $\boldsymbol{q}_x$ are the stable ($\boldsymbol{S}$) and unstable ($\boldsymbol{\mathcal{U}}$) manifolds, respectively. Points on S (red online, medium grey print) asymptotically approach $\boldsymbol{q}_x$ under the map, while points on $\boldsymbol{\mathcal{U}}$ (blue online, dark grey print) asymptotically approach $\boldsymbol{q}_x$ under the inverse map. Several escape and capture lobes are labeled. The eye-shaped region bounded by the segments of $\boldsymbol{S}$ and $\boldsymbol{\mathcal{U}}$ connecting the points $\boldsymbol{q}_x$ to $\boldsymbol{P}_0$ is called the complex. The oval-shaped curves (black online) centered about ($q = 0.62$, $p = 0$) are trapped orbits surrounding the stable fixed point that form a continent of stability. The points surrounding the continent of stability (cyan online, light grey print) lie within a chaotic sea. The vertical line segment (green online) represents a burst of trajectories launched from the boundary point $\boldsymbol{r}_0 = (0.3, 0.4067)$. Escape lobe E_i is the entire region bounded by $\boldsymbol{S}$ and $\boldsymbol{\mathcal{U}}$ between $\boldsymbol{P}_i$ and $\boldsymbol{Q}_i$, while capture lobe C_i is the entire region bounded by $\boldsymbol{S}$ and $\boldsymbol{\mathcal{U}}$ between $\boldsymbol{Q}_{i-1}$ and $\boldsymbol{P}_i$. See also the figures in Refs. [65] and [66].

At each reflection, we record the vector (q, p). Finally, if $q < 0$ (i.e. if the particle bounces off the lower boundary of the vase), we replace (q, p) with $(-q, -p)$. This is equivalent to propagating the trajectory within a vase in which the lower boundary is replaced by a horizontal mirror at $y = 0$. The vase dynamics induces a discrete mapping $\boldsymbol{\mathcal{M}}(q, p) = (q', p')$ in the new coordinates.

The mapping is not necessarily continuous in the concave part of the boundary (near the neck of the vase). Discontinuities arise when trajectories graze this part of the boundary (a grazing trajectory has

$$\boldsymbol{v}_{\text{outgoing}} \cdot \boldsymbol{T}(\boldsymbol{r}_{\text{graze}}) = \pm 1, \tag{5}$$

i.e. the velocity is parallel or antiparallel to the tangent to the boundary at the grazing point). However, we have chosen the shape of the vase such that any such discontinuities can only occur at the last reflection before escape. These discontinuities appear in the escape-time graph as discontinuities in the slope of the escape time, but the escape time itself is continuous at these points. There is also a second way that discontinuities in slope arise—when a trajectory encounters the point at which the vertical detector intersects either boundary wall (Fig. 3). In both of these cases, the number of reflections to escape changes by one (discontinuities in the escape time itself also arise, where it goes to infinity or where the trajectory does not escape.).

C. The homoclinic tangle and epistrophes

The organization of the chaotic dynamics is revealed by the discrete mapping $\boldsymbol{\mathcal{M}}(q, p)$, shown in Fig. 4. In this mapping, the SPO is transformed into a stable fixed point. Surrounding this point is a continent of stability, which is a set of trapped, quasiperiodic orbits centered near the point ($q = 0.62, p = 0$). A quasiperiodic orbit in the vase transforms into an oval-like curve in which points discretely move in a clockwise sense. A burst of trajectories launched in all directions from the boundary point $\boldsymbol{r}_0$ corresponds to the vertical line segment $\boldsymbol{\mathcal{L}}_0 = \{q_0 = 0.5607, -1 < p_0 < 1\}$. $\boldsymbol{\mathcal{L}}_0$ intersects the stable region resulting in trajectories that never escape. The presence of these stable orbits leads to breaks in the escape-time graph.

The UPO is transformed into an unstable fixed point, which we call $\boldsymbol{q}_x$ (see Fig. 4). Attached to this point are two special curves called the stable and unstable manifolds, $\boldsymbol{S}$ and $\boldsymbol{\mathcal{U}}$, respectively. These are invariant curves under the action of the map $\boldsymbol{\mathcal{M}}$. Under the action of $\boldsymbol{\mathcal{M}}$, points on the stable manifold (red online) asymptotically approach $\boldsymbol{q}_x$, while points on the unstable manifold (blue online) moving under the inverse map asymptotically approach $\boldsymbol{q}_x$. This induces a natural orientation to the stable and unstable manifolds, toward $\boldsymbol{q}_x$ on the stable manifold, and away from $\boldsymbol{q}_x$ on the unstable manifold. Neither the stable nor the unstable manifold can intersect itself.

The union of intersecting stable and unstable manifolds is called a homoclinic tangle [71]. We use the notation of our previous references to describe various segments of the manifolds and associated regions of the plane. We call the eye-shaped region bounded by the segments of $\boldsymbol{S}$ and $\boldsymbol{\mathcal{U}}$ connecting the points $\boldsymbol{P}_0$ and $\boldsymbol{q}_x$ the complex (some call this region the resonance zone). The region bounded by the segments of $\boldsymbol{S}$ and $\boldsymbol{\mathcal{U}}$ connecting $\boldsymbol{P}_0$ to $\boldsymbol{Q}_0$ is called escape lobe 0 and is denoted by E_0. The nth image of E_0 is $E_n = \boldsymbol{\mathcal{M}}^n(E_0)$ where n is any integer; it is bounded by the segments of $\boldsymbol{S}$ and $\boldsymbol{\mathcal{U}}$ connecting $\boldsymbol{P}_n = \boldsymbol{\mathcal{M}}^n(\boldsymbol{P}_0)$ and $\boldsymbol{Q}_n = \boldsymbol{\mathcal{M}}^n(\boldsymbol{Q}_0)$. The points $\boldsymbol{P}_n$ and $\boldsymbol{Q}_n$ are intersections of $\boldsymbol{S}$ and $\boldsymbol{\mathcal{U}}$, which are called homoclinic points. Similarly, we define capture lobe 0, denoted by C_0, which is bounded by the segments of $\boldsymbol{S}$ and $\boldsymbol{\mathcal{U}}$ connecting $\boldsymbol{Q}_{-1}$ with $\boldsymbol{P}_0$. The nth image of C_0 is $C_n = \boldsymbol{\mathcal{M}}^n(C_0)$, and it is bounded by the segments of $\boldsymbol{S}$ and $\boldsymbol{\mathcal{U}}$ connecting $\boldsymbol{Q}_{n-1}$ with $\boldsymbol{P}_n$.

The four lobes E_{-1} and C_1, which lie inside the complex, and E_0 and C_0, which lie outside the complex, form what is called a turnstile, and control how points enter and exit the complex. Since $E_0 = \mathcal{M}(E_{-1})$, points that land in E_{-1} exit the complex on the next iterate of the map. Similarly, since $C_1 = \mathcal{M}(C_0)$, points enter the complex by landing in C_0 and then in C_1 (the complex captures the points). From there, they map forward to C_2 and C_3, which lie entirely inside the complex, and then to C_4. A portion of this region intersects E_0, so points that fall into this region have entered and escaped the complex in four iterates. The minimum number of iterates that points remain in the complex (three in this case) is called the minimum delay time.

The vertical line segment in Fig. 4 (green online) represents a burst of trajectories (with initial momenta uniformly distributed) launched from the point $\boldsymbol{r}_0 = (0.3, 0.4067)$ on the upper boundary wall. If we record the time for the chaotic trajectories to escape the vase and arrive at the detector, we obtain the escape-time graph shown in Fig. 5(a). The vertical line of initial conditions in Fig. 4 intersects the complex, and if we record the number of iterates for the same trajectories to exit the complex, we obtain Fig. 5(b). We see that each icicle is rectified into a line segment, called an escape segment, that represents a set of trajectories that escape after the same number of bounces.

Let us focus on the segment labeled E_1. Trajectories in this segment exit the complex after four bounces. However, the trajectories must propagate further to escape the vase. Figure 3 shows the time and the number of bounces required for each trajectory in E_1 to escape the vase. A subset of this set of trajectories arrives at the detector after only four bounces, but others arrive after $4 + k$ bounces where k is any positive integer. If we compute the time spectrum of escaping trajectories, each escape segment, i.e. each icicle, produces a pulse of escaping trajectories. The whole burst of trajectories escapes the vase in an infinite sequence of pulses with each pulse representing a single icicle/escape segment.

Sequences of icicles are rectified into sequences of escape segments called epistrophes. The word epistrophe is a term from rhetoric meaning "a repeated ending following a variable beginning." Asymptotically, the tails of all epistrophes decrease at the same rate [65]. The set of escape segments can be partially predicted using the previously mentioned methods called homotopic lobe dynamics [25,66,67]. One of these methods will be applied in the accompanying paper [69] to generate a minimal topologically required subset of the fractal set of escape segments.

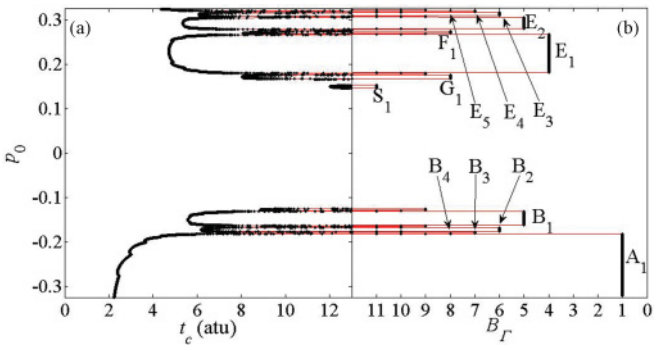

FIG. 5. (Color online) Continuous and discrete escape times for a burst of trajectories launched from (0.3, 0.4067). (a) Continuous escape time: the time required for trajectories to escape from the vase and arrive at a detector placed at $x = 1.5$. (b) Number of bounces required to exit the complex and land in escape lobe E_0. Sequences of escape segments, called epistrophes, have been labeled. (Note: epistrophe E with escape segments E_j must not be confused with escape lobes E_j).

III. ESCAPE TIME VERSUS DETECTOR POSITION

Here, we examine one of the quantities that can be most directly measured: the escape time versus the detector position. We first give a ray calculation, then use that ray calculation to compute a semiclassical wave function and its Fourier transform, and finally we show the results of an experiment using ultrasound.

A. Ray calculation

We launch a family of trajectories from the vase boundary point $\boldsymbol{r}_0$, and we stop them at the vertical line segment at $x = 1.5$ alu. For each escaping trajectory, we record the vertical detector position and the escape time [Fig. 6(a)]. We see that the signal consists of a complicated set of sawtooth oscillations. Each type of trajectory is plotted in a graph below the signal (plotted in the same colors online). The earliest trajectories to escape are the direct trajectories [Fig. 6(b), blue online]. This family is bounded by two grazing trajectories, which are also shown. As we rotate the initial velocity vector clockwise past the trajectory that grazes the lower lip, we encounter what we call the oscillatory rays [Fig. 6(c), black online]. These trajectories bounce through the vase's neck any number of times and then escape. Since these are encountered by rotating the direct trajectories continuously through a grazing trajectory, the sawtooth produced by the oscillatory trajectories is connected to the curve produced by the direct trajectories.

Next, we encounter the whispering gallery (WG) trajectories [Fig. 6(d), green online]. These trajectories hug the convex segments of the boundary walls. Clockwise WG trajectories

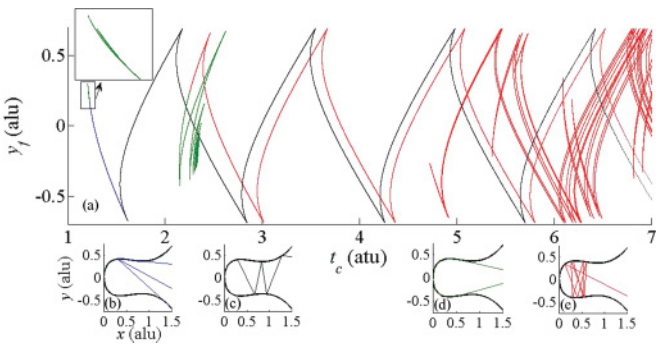

FIG. 6. (Color online) Detector position versus the escape time for a burst of trajectories launched from the boundary point (0.3, 0.4067). [In the online version, the colors correspond to the trajectories in (b)−(e).] (b) Rays that escape the vase without reflecting off either boundary (blue online). (c) Oscillatory rays (black online). (d) Whispering gallery (WG) trajectories (green online). (e) Chaotic trajectories (red online).

TABLE I. Initial conditions for the different types of trajectories contributing to the signal in Fig. 6. The first column contains the trajectory type. The second column contains initial conditions in the form of a polar angle measured with respect to a space-fixed Cartesian coordinate system with origin at the burst point. The third column gives the corresponding initial momentum. The first five rows contain the different types of trajectories and their ranges of initial conditions. The sixth and seventh rows contain initial conditions for the two grazing trajectories starting at (0.3, 0.4067). The last two rows give the initial conditions for the intersection of $\mathcal{L}_0$ and the complex's boundaries.

Trajectory	Initial polar angle (rad)	Initial momenta
Clockwise WG	$-0.0918 < \theta_0 < 0.1023$	$0.9812 < p_0 < 1$
Direct rays	$-0.734 < \theta_0 < -0.0918$	$0.6702 < p_0 < 0.9812$
Oscillatory	$-1.1417 < \theta_0 < -0.734$	$0.321 < p_0 < 0.6702$
Chaotic	$-1.7952 < \theta_0 < -1.1417$	$-0.321 < p_0 < 0.321$
Counterclockwise WG	$-3.0393 < \theta_0 < -1.7952$	$-1 < p_0 < -0.321$
Graze with upper wall	-0.0918	0.9812
Graze with lower wall	-0.734	0.6702
Stable boundary of complex	-1.1417	0.321
Unstable boundary of complex	-1.7952	-0.321

hug the upper boundary wall and escape early. These produce a narrow set of sawtooth oscillations that are connected to the curve produced by the direct trajectories [inset in Fig. 6(a)]. In fact, the clockwise WG trajectories and direct trajectories are separated by a trajectory that grazes the upper boundary. The counterclockwise WG trajectories start at the upper boundary, circulate counterclockwise, hug the lower boundary, and then escape. Their contribution to the signal starts around 2.2 arbitrary time units (atu).

Finally, we have the chaotic trajectories in Fig. 6(e) (red online). The earliest chaotic trajectories arrive at around 2.2 atu. At about 4.7 atu, we see two closely spaced oscillations starting. By 7 atu, many chaotic trajectories are arriving at the line detector resulting in a complicated signal. We conclude this section with Table I, which gives the initial conditions for the different types of trajectories we have just discussed.

B. Semiclassical wave approximation

Let us now construct a semiclassical approximation to the wave function along a line of detectors to the right of the UPO, at $x = 1.5$ alu. This semiclassical wave function is an approximation to a complex solution to the two-dimensional Helmholtz equation,

$$\left(\frac{\partial^2}{\partial x^2} + \frac{\partial^2}{\partial y^2} + k^2\right)\psi_k = 0, \tag{6}$$

subject to the following boundary condition near the source ($r \sim r_0$):

$$\psi_k(\boldsymbol{r}) \sim \frac{e^{ik|\boldsymbol{r}-\boldsymbol{r}_0|}}{\sqrt{k|\boldsymbol{r}-\boldsymbol{r}_0|}}. \tag{7}$$

Such a wave represents the Green's function for the Schrödinger wave equation. Its real or imaginary parts may represent sound waves or microwaves in the vase. To compute this wave function, we must identify trajectories going from a point source to a point detector by numerical interpolation of computed trajectories.

1. Interpolating classical trajectories

We computed a family of over 4 million trajectories to interpolate trajectories connecting source and detector points. For this set of escaping trajectories, we show a plot of final position along the detector vs initial momentum (Fig. 7). Figure 7 shows that $y_f(p_0)$ possesses a complicated set of oscillations. We see that globally, this curve is disconnected for p_0 near 0 and possesses many discontinuities in slope. The disconnection arises because $\mathcal{L}_0$ possesses a set of trapped orbits (compare to Figs. 2 and 4). We choose a detector point y_D and draw a horizontal line through $y_f(p_0)$ and numerically solve for those p_0 that satisfy

$$y_f(p_0) - y_D = 0. \tag{8}$$

To simplify the problem of numerically computing the zeros, we break up the curve at points of discontinuous slope. Each smooth segment of the curve contributes 0, 1, or 2 interpolated trajectories at the detector point. We apply the secant method to each smooth set to numerically compute the zeros of Eq. (8).

2. Computing the semiclassical wave function

The semiclassical wave function is given by

$$\psi(\boldsymbol{r}) = \sum_{j=1}^{N} A_j(\boldsymbol{r}) \frac{e^{ikr_0}}{\sqrt{r_0}} \exp\left[\frac{iS_j(\boldsymbol{r})}{\hbar} - \frac{i\mu_j\pi}{2}\right]. \tag{9}$$

This form of the wave function can be found in Ref. [72], where it was used in the construction of a model of electronic transport through a semiconductor microjunction. The sum

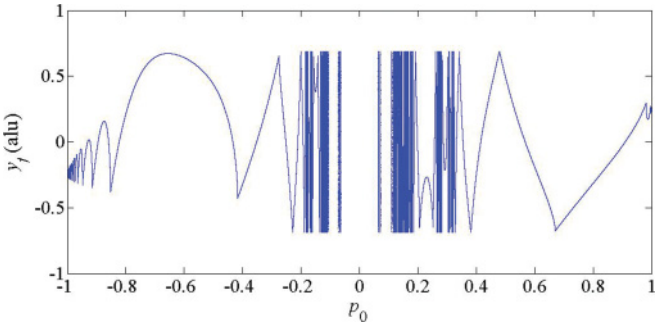

FIG. 7. (Color online) Detector position versus initial momentum for the source at $\boldsymbol{r}_0$.

runs over the interpolated trajectories connecting the source and detector points. Here, $A_j(\boldsymbol{r})$ is the amplitude of the wave function. This function is a ratio of the determinants of Jacobians in the representation $[x(t,\theta_j), y(t,\theta_j)]$ where x and y are the positions as a function of time and initial launch angle of the jth trajectory, that starts on a small circle of radius r_0 around the initial point. Here, $A_j(\boldsymbol{r})$ can be rewritten in terms of $\underset{\sim}{J}(t,\theta_j) = \frac{\partial(x,y)}{\partial(t,\theta_j)}$ [72–74],

$$|A_j(\boldsymbol{r})|^2 = \rho(\boldsymbol{r}) = \rho_0(r_0,\theta_j)\frac{\det[\underset{\sim}{J}(0,\theta_j)]}{\det[\underset{\sim}{J}(t,\theta_j)]}. \tag{10}$$

The initial Jacobian can be evaluated analytically:

$$\begin{aligned} &\frac{\partial x}{\partial t} = \cos(\theta_j), \quad \frac{\partial x}{\partial \theta_j} = -t\sin(\theta_j), \\ &\frac{\partial y}{\partial t} = \sin(\theta_j), \quad \frac{\partial y}{\partial \theta_j} = -t\cos(\theta_j), \quad \det[\underset{\sim}{J}(0,\theta_j)] = t. \end{aligned} \tag{11}$$

Using the fact that the speed is set to 1, the determinant evaluates to the radius of the initial circle, r_0.

For the denominator in Eq. (10), we can use a change of representation to write out a simple analytical expression:

$$\det[\underset{\sim}{J}(t,\theta_j)] = \left(\frac{\partial x}{\partial t}\right)_\theta \left(\frac{\partial y}{\partial \theta}\right)_t - \left(\frac{\partial x}{\partial \theta}\right)_t \left(\frac{\partial y}{\partial t}\right)_\theta = v_x \left(\frac{\partial y}{\partial \theta}\right)_x. \tag{12}$$

Then the amplitude for the jth term in the wave function evaluated at the detector point $\boldsymbol{r}_D$ is

$$A_j(r_D) = \frac{\sqrt{r_0}}{\sqrt{\left|v_x\left(\frac{\partial y}{\partial \theta}\right)_x\right|}}. \tag{13}$$

In practice, the denominator is computed using two trajectories: the interpolated trajectory from source to detector and a closely spaced neighbor. The factor $\sqrt{r_0}$ in the numerator cancels the corresponding factor in the denominator of Eq. (9), so the result is independent of r_0.

The function $S_j(\boldsymbol{r})$ is the classical action [72–74], and is given by

$$S_j(r) = \int \boldsymbol{p}(\boldsymbol{q})d\boldsymbol{q} = \hbar k L'_j. \tag{14}$$

L'_j is the length of the path from the initial small circle of radius r_0 around the source point to the detector. It can be combined with the factor e^{ikr_0} in Eq. (9) to give kL_j, where L_j is the full length from source to detector.

Finally, μ_j is the Maslov index of the jth trajectory. This index records phase shifts due to focal points and reflections [72–74]. For each hard-wall collision, the Maslov index is increased by two. For each focal point the interpolated trajectory encounters, the Maslov index is increased by one. To find focal points, we numerically evaluated $\det[\underset{\sim}{J}(t,\theta_j)]$ along an interpolated trajectory. We approximated the partial derivatives in Eq. (13) with finite differences $(\Delta x, \Delta y, \Delta\theta)$ using a trajectory slightly perturbed from the interpolated one. At a focal point, $\det[\underset{\sim}{J}(t,\theta_j)]$ changes sign by continuously passing through zero. Thus the Maslov index is equal to twice the number of bounces plus the number of continuous sign changes in $\det[\underset{\sim}{J}(t,\theta_j)]$ between bounces.

Now let us substitute our results into Eq. (9):

$$\psi(\boldsymbol{r}_D) = \sum_{j=1}^{N} \frac{e^{i[kL_j(r_D)-\pi/2]}}{\sqrt{|(v_x)_j(\partial y/\partial\theta)_{x_D}|}}. \tag{15}$$

The wave function is evaluated at the detector point $\boldsymbol{r}_D = (x_D, y_D)$ over an interval of wave numbers k. The Fourier variable conjugate to the wave number is a path length. Therefore, we compute the Fourier transform of Eq. (15):

$$\tilde{\psi}(L;\boldsymbol{r}_D) = \frac{1}{\sqrt{2\pi}}\int_{-\infty}^{\infty} dk e^{-ikL} \sum_{j=1}^{N} \frac{e^{i[kL_j(r_D)-(1/2)\mu_j\pi]}}{\sqrt{|(v_x)_j(\partial y/\partial\theta)_{x_D}|}}. \tag{16}$$

The sum over interpolated trajectories is finite and thus can be removed from the integrand. The denominator and the Maslov phase shift both come out of the integrand as each is independent of k. Immediately, we see that the integral is the Dirac delta function. Therefore, the Fourier transform of the semiclassical wave function is

$$\tilde{\psi}(L;r_D) = \frac{1}{\sqrt{2\pi}} \sum_{j=1}^{N} \frac{e^{-i(1/2)\mu_j\pi}}{\sqrt{|(v_x)_j(\partial y/\partial\theta)_{x_D}|}} \delta(L - L_j). \tag{17}$$

Our final result is a collection of peaks centered near the lengths of the classical trajectories with the amplitudes depending on the classical amplitude $A_j(\boldsymbol{r})$ and the phase shifts due to reflections and focal points.

For each detector point, we computed an approximation to Eq. (17) by computing the fast Fourier transform (FFT) of Eq. (15). We chose a range and stepsize in k consistent with what can be done in microwave experiments [19–22,75]. We assume that the maximum frequency of waves fed into the vase is 20 GHz, which corresponds to a wave number of $k_{\max} = 400\pi/3(\mathrm{m}^{-1})$. The frequency increment is 0.001 GHz, which corresponds to a stepsize of $2\pi 10^{-2}/3(\mathrm{m}^{-1})$. We assume the vase to be 1 m wide from the base to the detectors which results in the conversion 1 m = 1.5 alu. We consider 21 detectors equally spaced over the range −0.5 to 0.5 alu. For a wave function to be constructed from an interpolated trajectory, that trajectory must land within a distance of 1×10^{-8} alu of the detector point. We note that these parameters are also easily adapted to an equivalent ultrasound cavity experiment, which is discussed in a later section.

3. Results

We present two two-dimensional surface plots showing the path length spectrum, which we define as $|\tilde{\psi}(L, x_D = 1.5, y_D)|$ multiplied by an exponential factor,

$$\varphi_{fft}(L, x_D = 1.5, y_D) = e^{0.25L}|\tilde{\psi}(L, x_D = 1.5, y_D)|. \tag{18}$$

We found that the exponential factor in Eq. (18) amplifies and, hence, reveals the small peaks associated with longer trajectories without causing them to blow up too rapidly. The

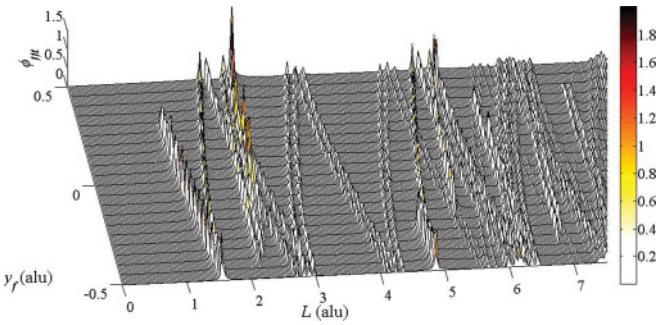

FIG. 8. (Color online) ϕ_{fft}, the amplified magnitude of the Fourier transform of the semiclassical wave function plotted for path lengths in the range 0 to 7.5 alu.

peaks centered at path lengths between 0 and 7.5 alu are shown in Fig. 8. The regions in which the surface appears to be discontinuous are due to cutoff of large values of ϕ_{fft}.

The most prominent aspect of this figure is the set of sawtooth oscillations similar to the oscillations seen in Fig. 6, indicating that (as expected) they will be visible in the Fourier transform of a steady-state experiment. The peaks between 1 and 1.5 alu are organized into a curve similar to the curve in Fig. 6 resulting from the direct rays. Between 2 and 2.25 alu, we see an accumulation of peaks where the counterclockwise whispering gallery trajectories accumulate. (However, our semiclassical calculation may not give an accurate description of the whispering gallery structure because we have included a finite number of trajectories and ignored diffraction.)

After the direct and whispering gallery trajectories have escaped, the intermediate to long path lengths result from the oscillatory and the chaotic trajectories. Figure 9 shows the path length spectrum for path lengths in the interval 7.5 to 15 alu.

4. Semiclassical calculation: Point detector at y = 0

Figures 8 and 9 give a global picture of the transmission probabilities for a vertical detector line past the vase's neck. We will now examine the signal at a single detector point $x = 1.5, y = 0$ alu, or for our simulation of a microwave experiment, $x = 1$ m. In Fig. 10, the first 16 peaks are shown together with the corresponding trajectories.

The first peak is obviously due to the direct trajectory. The second peak results from the first oscillatory trajectory. After this comes a cluster of eight peaks coherently interfering. Trajectory 3 may be regarded as the first in a sequence of

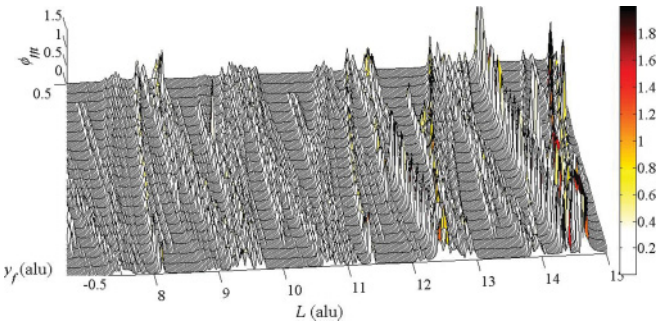

FIG. 9. (Color online) Same as Fig. 8 for path lengths in the range from 7.5 to 15 alu.

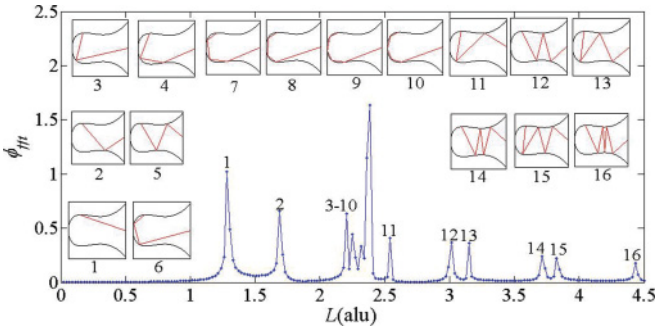

FIG. 10. (Color online) First 16 trajectories arriving at $y_D = 0$ and their corresponding peaks in the transmission spectrum.

counterclockwise whispering gallery trajectories (only counterclockwise whispering gallery trajectories are present at this detector point as the clockwise whispering gallery trajectories are focused into a narrow band at larger y). Trajectories 4 and 6 are also both whispering gallery trajectories that escape after two reflections, 7 and 8 after three reflections, and 9 and 10 after four reflections. Thus we see that whispering gallery trajectories from one source to one detector point exist in pairs having an equal number of reflections.

Trajectories 5, 12, 14, and 16 are oscillatory trajectories. Trajectories 11, 13, and 15 are the first chaotic trajectories to escape. They are members of the escape segment A_1 (see Fig. 5). Figure 11 shows the same path length spectrum over a wider range together with the first six trajectories arriving at the point detector from segment A_1.

Figure 12 shows the path length spectrum for path lengths 4.5 to 9 alu. Here, chaotic trajectories dominate the spectrum. Peaks associated with escape segments in the B, E, F, and G epistrophes (Fig. 5) are plainly visible (F and G peaks overlap because they have almost the same length).

IV. AN ULTRASOUND EXPERIMENT

A two-dimensional vase of the specified shape was constructed using two flat parallel aluminum plates separated by about 4.25 mm with the curved boundary formed from polytetrafluoroethelyene (PTFE) [76]. An ultrasound transducer was used as the point source, and a microphone was used as the point detector. Both devices are 40 kHz continuous-wave transducers damped with a coating of wax. With these

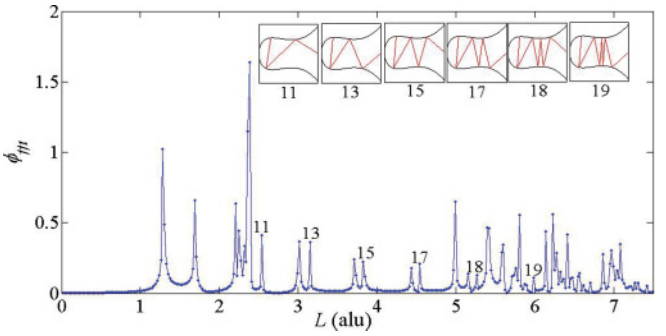

FIG. 11. (Color online) First six trajectories arriving at $y_D = 0$ from escape segment A_1 and their corresponding peaks in the transmission spectrum.

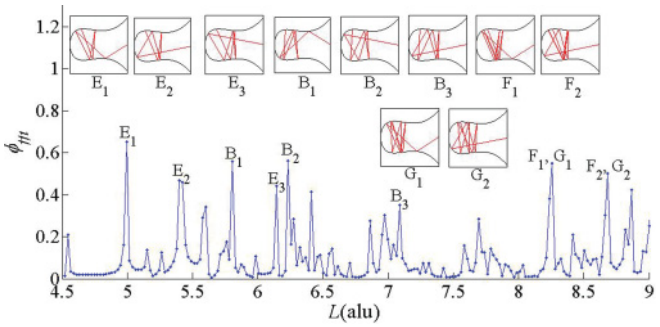

FIG. 12. (Color online) Path length spectrum for path lengths in the interval from 4.5 to 9 alu. The peaks corresponding to several escape segments are given the same labels as in Fig. 5. For each labeled escape segment, one interpolated trajectory is also presented.

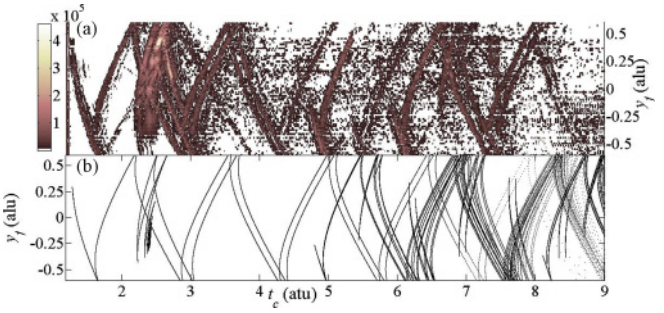

FIG. 13. (Color online) A comparison of the ultrasound experiment to the ray calculation. (a) The rescaled ultrasound signal between 1 and 9 atu with a t^3 time gain added. (b) The ray calculation.

modifications, we produced sound pulses about 0.2 ms in duration with a 43 kHz carrier wave. The position of the microphone was fixed, short pulses were emitted from the transducer, and the signal at the microphone was recorded as a function of time. Then the microphone was moved and the experiment repeated so that the escaping signal was recorded as a function of time and detector position. We will compare the escaping signal to a similar graph constructed by calculation of escaping trajectories.

To compare the simulation to the experimental results, we will rescale the latter into our arbitrary units. The PTFE vase is 87 cm along the horizontal direction. Setting 87 cm = 1.5 alu results in the conversion 0.0172 alu (cm^{-1}). To rescale the time units, we need the speed of sound in the air-space in the vase. We used the value 344.55 m(s^{-1}), which gives the conversion 1.6833 ms = 1 atu. For comparisons with our calculations, we scaled the experimentally measured signal and added a delay of 0.075 atu to the arrival times to account for delays in signal detection.

We compare the ray calculation to the recorded escaping ultrasound signal in the range from 1 to 9 atu in Fig. 13. Figure 13(a) shows the rescaled ultrasound signal, while Fig. 13(b) shows the simulation. The earliest signal detected (for $y \sim 0.45$ alu and $t \sim 1.3$ atu) corresponds to the direct and clockwise WG trajectories. This signal shows substantial diffraction into the classically forbidden or shadow region at larger y. Similarly, for $t \sim 2.3$ atu and $y \sim -0.35$ to 0.5 alu, there is very high intensity, corresponding to the counterclockwise WG trajectories.

This experiment does not resolve the complex structure starting near $t \sim 6.25$ atu, $y \sim 0$ alu (compare to Figs. 11 and 12), but many of the sawtooth oscillations associated with oscillating and chaotic trajectories are visible. We note that starting as early as 5 atu, attenuation and absorption in the vase walls has reduced the signal intensity. A time gain of t^3 was added to reveal the later time structure. Overall, there is respectable agreement between the experiment and the simulation.

V. SUMMARY

As stated in the introduction and in Ref. [68], the vase provides a simple model for studying chaotic transport. The vase possesses an unstable periodic orbit within the neck, all trajectories that pass through this orbit escape without return, and a graph of the time for trajectories to escape the vase displays a sensitive dependence on the initial conditions with an infinite number of icicles having structure within structure at all levels of resolution. By counting the number of bounces for trajectories to reach a certain region in the surface of section, the icicles in the escape-time graph are rectified into escape segments or sets of trajectories that escape after the same number of bounces.

Measurements on such a system could be carried out in either the time domain or the frequency domain. For the frequency domain, we carried out a calculation of the Green's function for the Schroedinger equation. Its Fourier transform gives results similar to those of computations in the time domain for pulsed sources.

A graph of the detector position versus the escape time shows a complicated set of sawtooth oscillations related to oscillating and chaotic trajectories. A macroscopic vase was constructed, and an ultrasound measurement was carried out, and respectable agreement was found between computations and measurements. The early part of the fractal structure is plainly visible in these experiments. Higher-resolution measurements, for example, using light or microwaves, should reveal deeper parts of the fractal.

In the accompanying paper, we will apply one of the recently developed improvements to homotopic lobe dynamics to analyze the fractal structure of the escape-time graph for this system.

ACKNOWLEDGMENT

This work was supported by the National Science Foundation (NSF).

[1] C. C. Rankin and W. H. Miller, J. Chem. Phys. **55**, 3150 (1971).
[2] A. Tiyapan and C. Jaffé, J. Chem. Phys. **103**, 5499 (1995).
[3] C. Jaffé, D. Farrelly, and T. Uzer, Phys. Rev. A **60**, 3833 (1999).
[4] C. Jaffé, D. Farrelly, and T. Uzer, Phys. Rev. Lett. **84**, 610 (2000).
[5] T. Uzer, C. Jaffe, J. Palacian, P. Yanguas, and S. Wiggins, Nonlinearity **15**, 957 (2002).

[6] S. Müller, S. Heusler, P. Braun, and F. Haake, New J. Phys. **9**, 12 (2007).
[7] P. Gaspard and J. R. Dorfman, Phys. Rev. E **52**, 3525 (1995).
[8] P. Gaspard and R. Klages, Chaos **8**, 409 (1998).
[9] H. G. L. Schwefel, H. E. Tureci, A. D. Stone, and R. K. Chang, in *Progress in Asymmetric Resonant Cavities: Using Shape as a Design Parameter in Dielectric Microcavity Lasers* in Optical Microcavities, edited by K. Vahala (World Scientific, 2004), p. 415.
[10] J. U. Nockel and A. D. Stone, Nature **385**, 45 (1997).
[11] A. Mekis, J. U. Nöckel, G. Chen, A. D. Stone, and R. K. Chang, Phys. Rev. Lett. **75**, 2682 (1995).
[12] S. Chang, R. K. Chang, A. D. Stone, and J. U. Nöckel, J. Opt. Soc. Am. B **17**, 1828 (2000).
[13] E. E. Narimanov, G. Hackenbroich, P. Jacquod, and A. D. Stone, Phys. Rev. Lett. **83**, 4991 (1999).
[14] A. D. Stone, Physica A (Amsterdam) **288**, 130 (2000).
[15] A. D. Stone, Phys. Scr., T **90**, 248 (2001).
[16] H. E. Tureci, H. G. L. Schwefel, P. Jacquod, and A. D. Stone, Prog. Opt. **47**, 75 (2005).
[17] J. U. Nockel and A. D. Stone, in *Chaotic Light: A Theory of Assymetric Resonant Cavities* in Optical Processes in Microcavities, edited by R. K. Chang and A. J. Campillo (World Scientific, 1996), p. 389.
[18] A. D. Stone and J. U. Noeckel, J. Acoust. Soc. Am. **101**, 3115 (1997).
[19] S. Sridhar, Phys. World **14**, 23 (2001).
[20] W. Lu, M. Rose, K. Pance, and S. Sridhar, Phys. Rev. Lett. **82**, 5233 (1999).
[21] W. Lu, L. Viola, K. Pance, M. Rose, and S. Sridhar, Phys. Rev. E **61**, 3652 (2000).
[22] W. T. Lu, K. Pance, P. Pradhan, and S. Sridhar, Phys. Scr., T **90**, 238 (2001).
[23] W. T. Lu, S. Sridhar, and M. Zworski, Phys. Rev. Lett. **91**, 154101 (2003).
[24] S. Sridhar and W. Lu, J. Stat. Phys. **108**, 755 (2002).
[25] K. A. Mitchell, Physica D **238**, 737 (2009).
[26] K. Burke and K. A. Mitchell, Phys. Rev. A **80**, 033416 (2009).
[27] K. A. Mitchell and D. A. Steck, Phys. Rev. A **76**, 31403 (2007).
[28] D. M. Wang and J. B. Delos, Phys. Rev. A **63**, 43409 (2001).
[29] S. Freund, R. Ubert, E. Flöthmann, K. Welge, D. M. Wang, and J. B. Delos, Phys. Rev. A **65**, 53408 (2002).
[30] J. Delos and K. Mitchell, Few-Body Syst. **38**, 181 (2006).
[31] K. A. Mitchell, J. P. Handley, B. Tighe, A. Flower, and J. B. Delos, Phys. Rev. Lett. **92**, 73001 (2004).
[32] K. A. Mitchell, J. P. Handley, B. Tighe, A. Flower, and J. B. Delos, Phys. Rev. A **70**, 43407 (2004).
[33] K. A. Mitchell and J. B. Delos, Physica D **229**, 9 (2007).
[34] J. Ottino, A. Souvaliotis, and G. Metcalfe, Chaos Solitons Fractals **6**, 425 (1995).
[35] T. Shinbrot, L. Bresler, and J. M. Ottino, Physica D **93**, 191 (1996).
[36] G. Fountain, D. Khakhar, I. Mezic, and J. Ottino, J. Fluid Mech. **417**, 265 (2000).
[37] J. M. Ottino, J. Fluid Mech. **417**, 265 (2000).
[38] K. M. Hill, N. Jain, and J. M. Ottino, Phys. Rev. E **64**, 11302 (2001).
[39] M. Horner, G. Metcalfe, S. Wiggins, and J. Ottino, J. Fluid Mech. **452**, 199 (2002).
[40] S. Wiggins and J. M. Ottino, Philos. Trans. R. Soc. London, Ser. A **362**, 937 (2004).
[41] S. C. Jana, G. Metcalfe, and J. M. Ottino, J. Fluid Mech. **269**, 199 (1994).
[42] L. P. Kouwenhoven, C. M. Marcus, P. L. McEuen, S. Tarucha, R. M. Westervelt, and N. S. Wingreen, Mesoscopic Electron Transport **345**, 16 (1997).
[43] C. Marcus, S. Patel, A. Huibers, S. Cronenwett, M. Switkes, I. Chan, R. Clarke, J. Folk, S. Godijn, and K. Campman, Chaos Solitons Fractals **8**, 1261 (1997).
[44] J. A. Folk, S. R. Patel, K. M. Birnbaum, C. M. Marcus, C. I. Duruöz, and J. S. Harris Jr, Phys. Rev. Lett. **86**, 2102 (2001).
[45] L. Zapanta, C. S. Poon, D. White, C. Marcus, and E. Katz, in *Engineering in Medicine and Biology Society, 2004. IEMBS'04. 26th Annual International Conference of the IEEE* (2004). Available electronically from IEEE.
[46] M. Bakhtiari, P. Vignolo, and M. Tosi, Physica E **28**, 385 (2005).
[47] P. Jung, J. G. Kissner, and P. Hänggi, Phys. Rev. Lett. **76**, 3436 (1996).
[48] J. L. Mateos, Physica A (Amsterdam) **325**, 92 (2003).
[49] H. Schanz, T. Dittrich, and R. Ketzmerick, Phys. Rev. E **71**, 26228 (2005).
[50] J. L. Mateos, Phys. Rev. Lett. **84**, 258 (2000).
[51] H. Schanz, M. F. Otto, R. Ketzmerick, and T. Dittrich, Phys. Rev. Lett. **87**, 70601 (2001).
[52] H. Yang and Z. Liu, J. Phys. Oceanogr. **27**, 1258 (1997).
[53] P. D. Miller, L. J. Pratt, K. R. Helfrich, and C. K. R. T. Jones, J. Phys. Oceanogr. **32**, 80 (2002).
[54] M. V. Budyansky, M. Y. Uleysky, and S. V. Prants, J. Exp. Theor. Phys. **99**, 1018 (2004).
[55] M. V. Budyansky, M. Y. Uleysky, and S. V. Prants, e-print arXiv:nlin/0507020 (to be published).
[56] M. V. Budyansky and S. V. Prants, in *ASME Conf. Proc.: 20th Biennial Conference on Mechanical Vibration and Noise* (2005), p. 189. Available electronically from ASME.
[57] M. V. Budyansky, M. Y. Uleysky, and S. V. Prants, Commun. Nonlinear Sci. Numerical Simulation **12**, 31 (2007).
[58] S. Prants, M. Budyansky, M. Y. Uleysky, and G. Zaslavsky, Chaos **16**, 033117 (2006).
[59] C. Jaffé, S. D. Ross, M. W. Lo, J. Marsden, D. Farrelly, and T. Uzer, Phys. Rev. Lett. **89**, 11101 (2002).
[60] C. Jaffé and T. Uzer, Nucl. Phys., Section A **737**, 125 (2004).
[61] C. Jaffé and T. Uzer, Ann. N.Y. Acad. Sci. **1017**, 39 (2004).
[62] B. B. Mandelbrot, *The Fractal Geometry of Nature* (W. H. Freeman Company, New York, 1982).
[63] L. Keen, R. L. Devaney, and K. T. Alligood, *Chaos and Fractals: The Mathematics Behind the Computer Graphics* (American Mathematical Society, Providence, R. I., 1989).
[64] M. F. Barnsley, *Fractals Everywhere* (Academic Press, Boston, 1993).
[65] K. Mitchell, J. Handley, B. Tighe, J. Delos, and S. Knudson, Chaos **13**, 880 (2003).
[66] K. Mitchell, J. Handley, J. Delos, and S. Knudson, Chaos **13**, 892 (2003).
[67] K. A. Mitchell and J. B. Delos, Physica D **221**, 170 (2006).
[68] P. Hansen, K. A. Mitchell, and J. B. Delos, Phys. Rev. E **73**, 66226 (2006).
[69] J. A. Novick and J. B. Delos, Phys. Rev. E **85**, 016206 (2012).

[70] See Supplemental Material at http://link.aps.org/supplemental/10.1103/PhysRevE.85.016205 for numerically computing trajectories in the vase.
[71] S. Wiggins, *Introduction to Applied Nonlinear Dynamical Systems and Chaos* (Springer Verlag, New York, 2003).
[72] C. D. Schwieters, J. A. Alford, and J. B. Delos, Phys. Rev. B **54**, 10652 (1996).
[73] V. Maslov and M. Fedoriuk, *Semi-Classical Approximation in Quantum Mechanics* (Kluwer Academic Publishers, Dordrecht, Holland, 1981).
[74] J. B. Delos, Adv. Chem. Phys. **65**, 161 (1986).
[75] K. Pance, W. Lu, and S. Sridhar, Phys. Rev. Lett. **85**, 2737 (2000).
[76] Commonly known by its trade name, Teflon.